Cell Reports
Physical Science

Article

Hierarchically porous graphitized carbon membrane for 1-Watt-hour-class rechargeable lithium-oxygen pouch cells

Graphical abstract

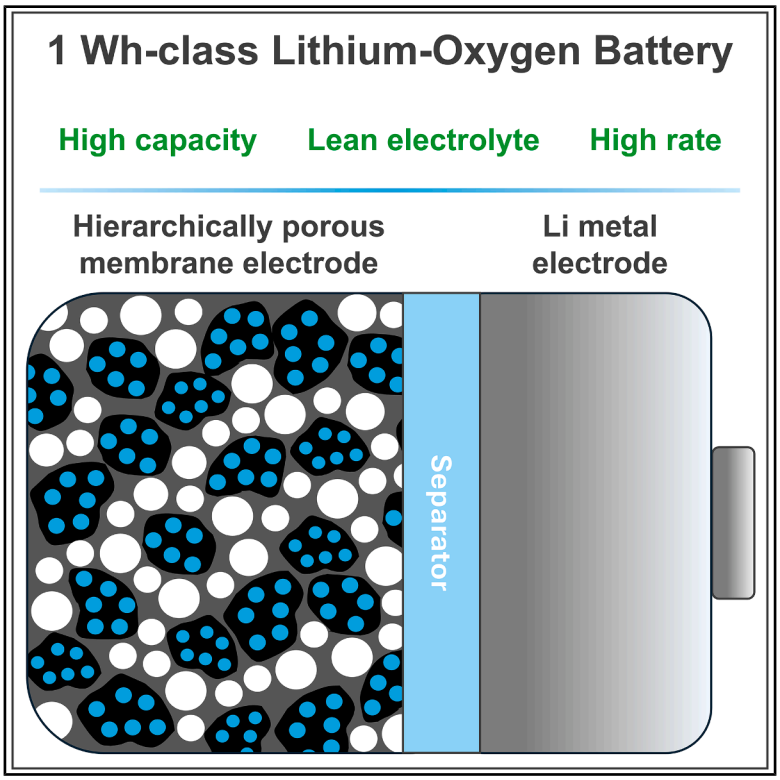

Authors

Arghya Dutta, Takashi Kameda, Emiko Mizuki, ..., Yuuka Nakajima, Takahiro Morishita, Shoichi Matsuda

Correspondence

dutta.arghya@nims.go.jp (A.D.), matsuda.shoichi@nims.go.jp (S.M.)

In brief

Dutta et al. develop scalable, self-standing carbon membranes with hierarchical porosity for lithium-oxygen batteries (LOBs). The electrodes enable high-rate, lean-electrolyte cycling and power a 1-Wh-scale multi-stacked pouch cell, advancing practical LOB technologies.

Highlights

- Scalable fabrication of self-standing porous carbon membranes
- Interconnected macropores for better O_2 transport
- Stable LOB cycling over 150 cycles at 1.5 mA cm^{-2} with lean electrolyte
- Multi-stacked LOB pouch cell demonstrates >1 Wh energy and long stability

Dutta et al., 2025, Cell Reports Physical Science 6, 102841
September 17, 2025
https://doi.org/10.1016/j.xcrp.2025.102841

CellPress

Cell Reports
Physical Science

CellPress
OPEN ACCESS

Article

Hierarchically porous graphitized carbon membrane for 1-Watt-hour-class rechargeable lithium-oxygen pouch cells

Arghya Dutta,[1,*] Takashi Kameda,[1] Emiko Mizuki,[1] Taiga Ozawa,[1] Shoji Yamaguchi,[1] Junji Takada,[2] Yuuka Nakajima,[2] Takahiro Morishita,[2] and Shoichi Matsuda[1,2,3,4,*]

[1]Center for Green Research on Energy and Environmental Materials, National Institute for Materials Science, 1-1 Namiki, Tsukuba, Ibaraki 305-0044, Japan

[2]Kondo Teruhisa Memorial Advanced Carbon Technology Center, Toyo Tanso Co., Ltd., 5-7-12 Takeshima, Nishiyodogawa-ku, Osaka 555-0011, Japan

[3]Center for Advanced Battery Collaboration, National Institute for Materials Science, 1-1 Namiki, Tsukuba, Ibaraki 305-0044, Japan

[4]Lead contact

*Correspondence: dutta.arghya@nims.go.jp (A.D.), matsuda.shoichi@nims.go.jp (S.M.)

https://doi.org/10.1016/j.xcrp.2025.102841

SUMMARY

Despite lithium-oxygen batteries (LOBs) achieving energy densities over 500 Watt hours (Wh) kg^{-1} at the cell level, challenges remain in extending cycle life, high-rate operation, and scalability. A critical limitation lies in designing carbon-based positive electrodes with optimal porosity and stability. Previous efforts with highly porous carbon materials face issues like unoptimized pore structures, excessive microporosity, low stability, and non-scalable fabrication methods, particularly under lean-electrolyte conditions. Here, we report a scalable, cost-effective approach to fabricate self-standing carbon membranes via (1) hard-templated synthesis of mesoporous carbon with reduced microporosity, (2) slurry casting using the doctor-blade method, and (3) non-solvent-induced phase separation (NIPS) to create interconnected macropores for improved oxygen transport. LOB cells employing these hierarchically porous carbon membranes and lean electrolyte demonstrated stable cycling for over 150 cycles at 1.5 mA cm^{-2}. Additionally, a 1-Wh-class multi-stacked LOB achieved long cycling stability. This report offers a breakthrough in scalable, high-energy-density LOB electrode development.

INTRODUCTION

The realization of nonaqueous lithium-oxygen batteries (LOBs) having cell-level energy density >500 Watt hours (Wh) kg^{-1} requires the successful implementation of high-capacity electrodes (>4 mAh cm^{-2}) with lean electrolyte (<10 g Ah^{-1}).[1–3] However, achieving LOBs with both high energy density and long cycle life remains a significant challenge.[1,4] An important key factor in achieving improved performance lies in the design and optimization of the carbon structure employed as the positive electrode material.[5–18] The carbon electrode in LOBs serves multiple roles, providing a platform for the deposition and decomposition of lithium peroxide (Li_2O_2) during discharge and recharge processes ($2Li^+ + O_2 + 2e^- \leftrightarrow Li_2O_2$) while also facilitating efficient charge transfer and oxygen (O_2) diffusion and influencing the cycle life of the cell.[7]

For the development of porous carbon-based positive electrodes, precise control of the multi-scale pore structure is essential. It is widely acknowledged that both a large pore volume and a high surface area in the carbon material, which provide ample space for Li_2O_2 accommodation, contribute to increased battery capacity.[6,8,19,20] However, our recent analytical studies have revealed that, while a high surface area and large pore volume do enhance capacity, the significant amount of electrolyte required to fill the pores can adversely affect the overall energy density of the battery.[1] This issue is exacerbated when the porous carbon materials contain a large fraction of micropores (<2 nm in diameter) that, although they can be penetrated by the electrolyte, remain inactive during the discharge process.[21,22] For this reason, to develop carbon electrodes optimized for high-energy-density LOBs, it is crucial to minimize the presence of the micropores. In contrast, mesopores (2–50 nm in diameter) play an active role in accommodating Li_2O_2, which forms during the discharge process.[23,24] Additionally, macropores (>50 nm) are advantageous for providing efficient pathways for mass transport of both O_2 and Li ions, supporting effective electrochemical reactions even at high current densities. Therefore, an optimized carbon electrode structure with reduced microporosity and a well-defined hierarchical network of mesopores and macropores is ideal for achieving high energy density in LOBs.

In addition to the carbon pore structure, the presence of surface functional groups and the degree of graphitization significantly influence the capacity, energy efficiency, and cycle life of LOBs.[25,26] It is well established that the decomposition of

carbon materials during cycling, particularly in electrodes containing oxygen functional groups, is a primary contributor to poor cycle life.[25] Besides, this degradation becomes more pronounced under lean-electrolyte conditions.[27] In contrast, carbon materials treated at high temperatures exhibit improved stability as LOB electrodes. For instance, defect-free graphene with a well-defined mesopore structure has shown superior LOB performance, achieving long cycle stability (>260 cycles) at a current density of 0.4 mA cm^{-2}.[28] However, these nanostructured carbon materials often lack macroscopic interconnected pores, which limits their effectiveness under higher current densities (>1 mA cm^{-2}). Moreover, for the development of large-scale practical LOBs, it is essential to fabricate such porous carbon electrodes using cost-effective and scalable methods.

In this study, we developed scalable and cost-effective techniques for fabricating self-standing carbon membranes using a three-step procedure: (1) hard-template-based synthesis of carbon powder with a defined mesopore structure, (2) slurry casting via the doctor-blade method to create self-standing membranes, and (3) non-solvent-induced phase separation (NIPS) to form interconnected macropores that facilitate efficient oxygen and Li-ion transport through the membrane. First, carbon powder was synthesized using a hard-templating method, employing phenolic resin as the carbon precursor and magnesium oxide (MgO) as the hard template.[29] By adjusting the MgO template size, we precisely controlled the mesopore dimensions. A secondary heat treatment was performed at five different temperatures to further refine the surface functionalities and minimize the microporosity of the carbon materials. Following this, large, self-standing carbon membranes with uniform thickness were fabricated using a procedure developed in our group.[30] This process combines slurry casting via the doctor-blade method with the NIPS technique, producing carbon membranes with a hierarchical macro-mesoporous interconnected network.[31,32] The resulting LOB cells, which incorporated these synthesized porous carbon membranes as positive electrodes, underwent extensive performance testing and degradation analysis. These tests demonstrated the novelty of the developed carbon electrodes, showing long cycle life and high-current-density performance (>150 cycles at 1.5 mA cm^{-2}). Additionally, we achieved successful cycling of 1-Wh-class LOBs, marking a significant advancement toward the practical application of this technology. The methodologies and results presented in this study offer great potential for the development of next-generation, high-energy-density LOBs.

RESULTS AND DISCUSSION

Synthesis and characterization of MgO templated carbon powder

Nanoporous carbon materials were synthesized using a hard-templating method with phenol resin as the carbon precursor and MgO as the hard template. This approach allows for the convenient control of the mesopore size of the resulting carbon material by adjusting the size of the MgO template.[29] The synthesis process (Figure 1A) involved a heat treatment of the phenol resin and MgO composite at 900°C under an inert atmosphere, leading to the carbonization of the precursor. Subsequently, the MgO template was selectively dissolved using a diluted acid at room temperature, resulting in the isolation of the carbon structure. To further tailor the properties of the carbon material, a secondary heat treatment was performed at five distinct temperatures: 1,000°C, 1,600°C, 1,900°C, 2,100°C, and 2,400°C. The resulting samples carbonized at these different temperatures are denoted as C-10, C-16, C-19, C-21, and C-24, respectively. This final heating step allowed for the modification of both the porosity and surface functionalities of the nanoporous carbon material.

The physicochemical properties of the porous carbon materials were thoroughly investigated using several analytical techniques. Scanning electron micrography (SEM) (Figure 1B) reveals that the carbon materials exhibit a particle-like morphology with sizes distributed over several micrometers. Notably, there is no clear morphological difference between samples. However, a clear enhancement of graphitization in carbon materials as a result of increasing carbonization temperature can be directly visualized through high-resolution transmission electron micrography (TEM) (Figure 1C). The micrographs for the carbon samples C-10 and C-16 exhibit highly disordered structures. As the carbonization temperature increases, the visual appearance of graphitic layers becomes evident in sample C-19, signifying an intermediate level of graphitization. Notably, samples C-21 and C-24 exhibit more pronounced and well-defined graphitic structures with higher crystallinity, representing a significant improvement in graphitization. Besides, the TEM images provide valuable insights into the overall structure of the carbon materials, revealing an intertwined assembly of two-dimensional carbon flakes.

Nitrogen (N_2) adsorption and desorption measurements at −196°C were performed to determine the surface area, pore volume, and pore diameter of the carbon powders. The results from the N_2 adsorption/desorption isotherms (Figure S1) and Barrett-Joyner-Halenda (BJH) pore-size distribution curves (Figure S2) reveal a gradual decrease in Brunauer-Emmett-Teller (BET) surface area with increasing carbonization temperature, while maintaining a mesoporous structure with pore diameters in the range of 9–10 nm. The surface area decreases as follows: C-10 (1,663 m^2 g^{-1}) > C-16 (1,651 m^2 g^{-1}) > C-19 (1,480 m^2 g^{-1}) > C-21 (1,070 m^2 g^{-1}) > C-24 (335 m^2 g^{-1}). A detailed pore analysis reveals trends in the volumes of micropores (<2 nm), small mesopores (2–20 nm), and large mesopores (>20 nm) (Table S1). The analysis indicates a significant reduction in both micropore and small-mesopore volumes with increasing carbonization temperature, while the volume of large mesopores remains relatively unchanged.

The Raman spectra provide valuable insights into the systematic changes in the intensity ratio of the D and G bands (I_D/I_G ratio) at various carbonization temperatures. The D band (1,350 cm^{-1}) represents vibrations of sp^3-bonded carbon atoms or defects, while the G band (1,580 cm^{-1}) corresponds to sp^2-bonded carbon atoms in a more graphitized carbon structure (Figure 1D).[33] Thus, the I_D/I_G intensity ratio serves as an indicator of the degree of graphitization and ordering within the carbon structure, with higher values indicating a more disordered structure. Notably, the I_D/I_G ratio decreases and the D and G bands become narrower as the carbonization temperature increases

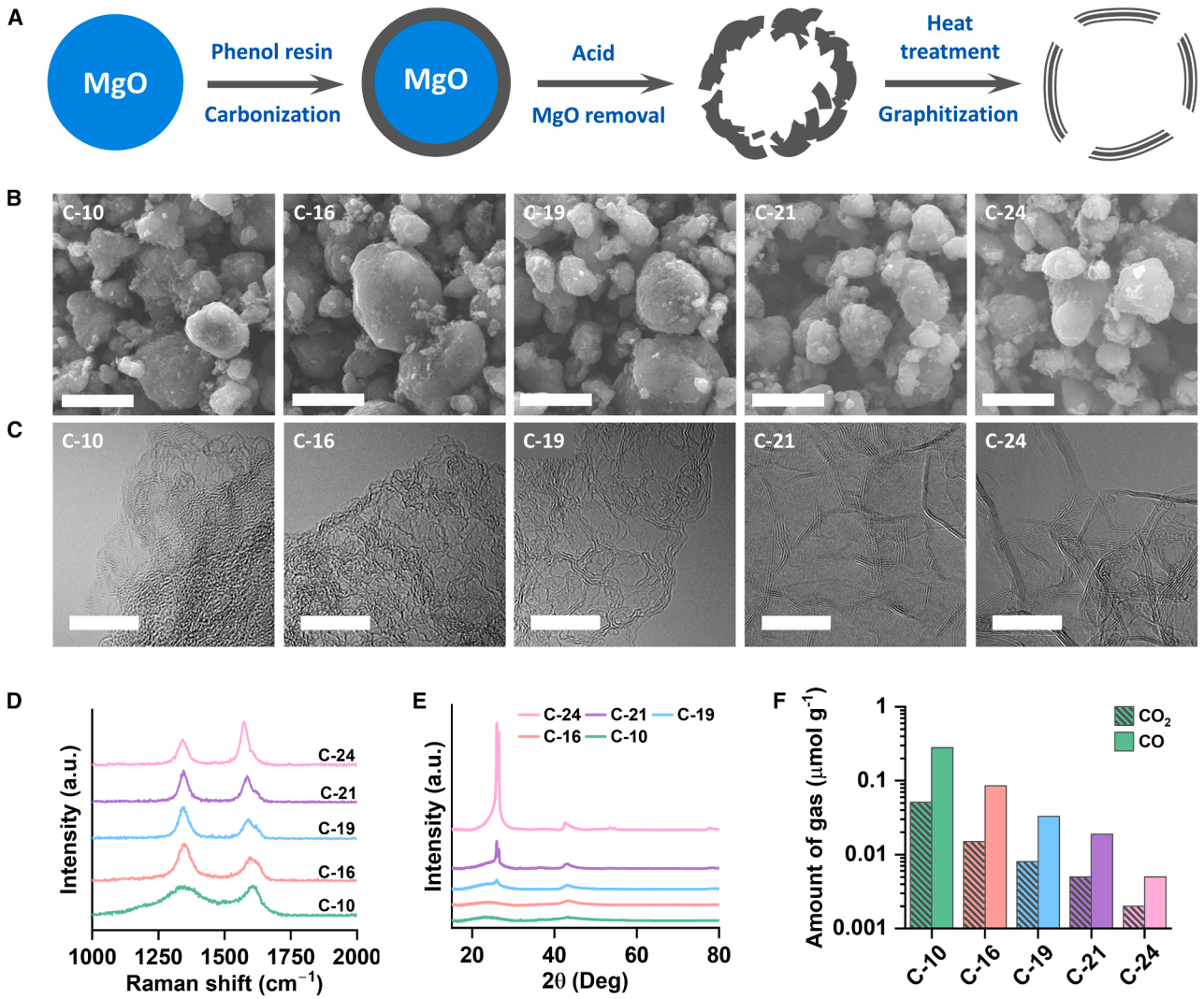

Figure 1. Synthesis process and physical characterizations of porous carbon powders

(A) Schematic representation of the synthesis procedure of the carbon powders.

(B–F) (B) SEM images, (C) TEM images, (D) Raman spectra, (E) XRD data, and (F) TPD data of the synthesized carbon powder samples. Scale bars in (B), 5 μm and (C), 10 nm.

(Figure S3). This indicates a gradual improvement in the ordering of the carbon structures.

The X-ray diffraction (XRD) patterns (Figure 1E) of the carbon samples give additional evidence for the development of a graphitic structure with increasing carbonization temperature. The XRD patterns of the carbons exhibit the appearance of a notable diffraction peak at $2\theta = 24^{\circ}$, corresponding to the (002) crystallographic plane of graphite crystallites when the carbonization temperature reaches 1,900°C. As the carbonization temperature rises, both the intensity and sharpness of this peak gradually enhance, and a new peak emerges at 43°, indicative of the (100) graphite plane. The primary Bragg reflection (002) peak demonstrates the development of a turbostratic graphitic structure, accompanied by a reduction in d-spacing with increasing carbonization temperature Figure S4). Notably, the XRD results unequivocally indicate a prominent increase in crystallinity in the samples when the carbonization temperature goes over 1,900°C.

For the quantitative assessment of carbon content, we performed carbon-hydrogen-nitrogen (C-H-N) analysis. Notably, as the carbonization temperature increases, there is a consistent upward trend in the carbon content (Figure S5). Since there is no nitrogen source in the carbon precursor, this observation suggests that higher-temperature carbonization progressively reduces the hydrogen content in the carbon, which indirectly indicates a lower oxygen content on the carbon surface. In general, as-synthesized carbon materials are known to possess varying quantities of oxygen functional groups, depending on the carbonization temperature. With an increase in carbonization temperature, the quantity of oxygen functional groups tends to decrease. To precisely estimate the oxygen functionalities present in the carbon materials carbonized at

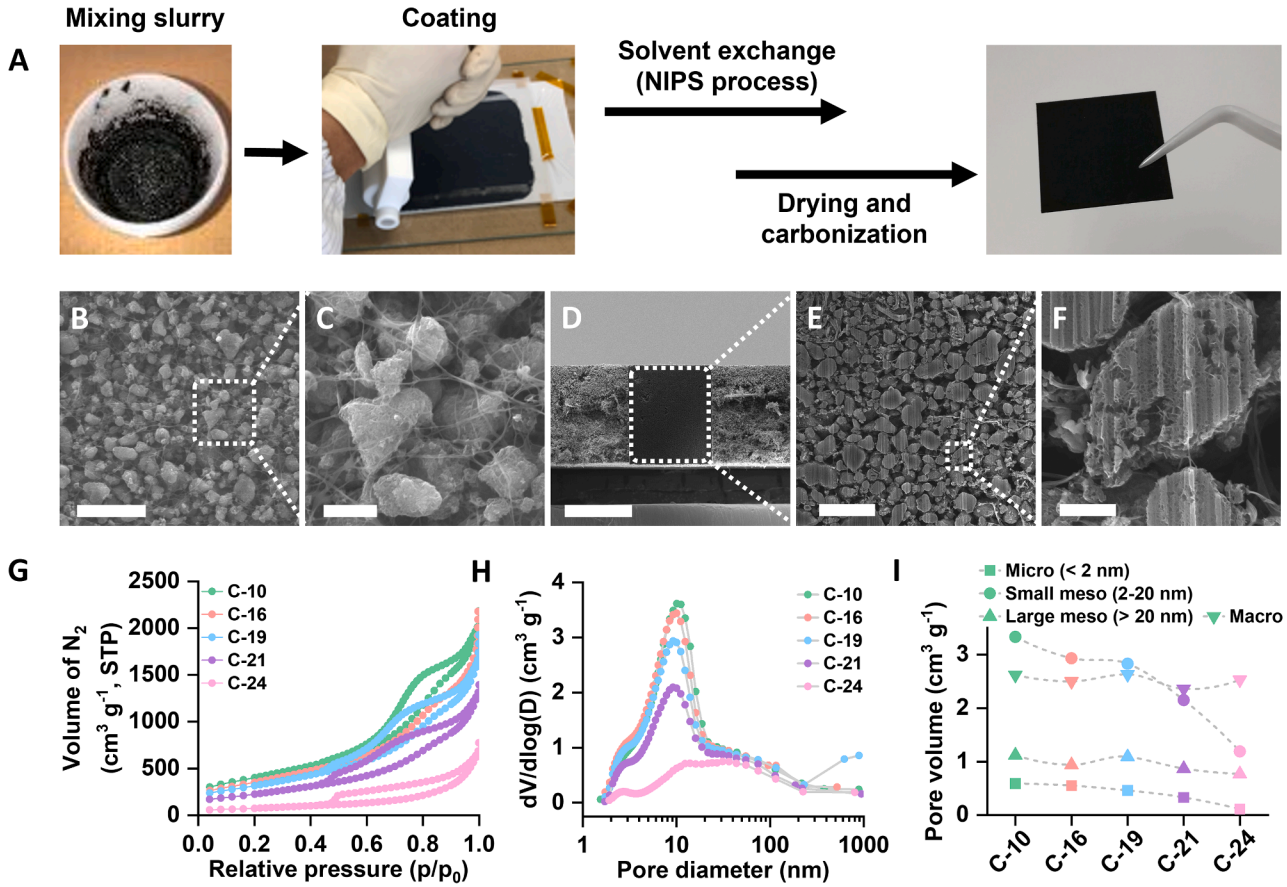

Figure 2. Fabrication process and physical characterizations of porous carbon membranes

(A) Schematic description of the fabrication process for free-standing electrodes.

(B–F) Top-view and (D–F) cross-section SEM images of C-21 as a representative of the free-standing electrodes. Scale bars, (B) 10 μm, (C) 2 μm, (D) 200 μm, (E) 10 μm, and (F) 1 μm.

(G and H) (G) N_2 adsorption/desorption isotherms and (H) BJH pore-size distribution curves of the membrane electrodes.

(I) Comparison of pore volumes across different diameter ranges for all membrane electrodes.

different temperatures, we conducted a temperature-programmed desorption (TPD) analysis. This method evaluates the desorption of gases during a temperature-programmed heat treatment of the samples. The results from the TPD analysis show the amounts of carbon dioxide (CO_2) and carbon monoxide (CO) desorbed from the five different carbon materials when heated up to 1,000°C (Figure 1F). The TPD data clearly demonstrate a consistent decrease in the amounts of both CO_2 and CO with increasing carbonization temperature. These results provide strong evidence of reduced oxygen functionalities in the materials treated at higher temperatures. Furthermore, we carried out a qualitative analysis of the oxygen-containing functional groups using X-ray photoelectron spectroscopy (XPS). The XPS C1s spectra reveal the presence of C−O functional groups (such as phenol, ether, and epoxy) at approximately 286.0 ± 0.1 eV, as well as C=O functional groups (such as carbonyl and quinone) at around 287.0 ± 0.2 eV (Figure S6).[25,26] The corresponding peaks in the O1s spectra are assigned to these functional groups as well (Figure S7).

Fabrication and characterization of self-standing porous carbon membrane

The self-standing carbon membranes were fabricated using the synthesized porous carbon powders through a slurry casting method combined with an NIPS process developed in our research group (Figure 2A).[30] This approach is advantageous for scalability, allowing the production of large-sized membranes suitable for LOB electrodes. The slurry was prepared by mixing the synthesized porous carbon powders, carbon fibers, carbon nanotubes (CNTs), and polyacrylonitrile (PAN) in N-methyl-2-pyrrolidone (NMP) solvent. The addition of carbon fibers and CNTs provided mechanical strength to the membrane. A typical slurry composition consisted of 75 wt % carbon powder, 5 wt % carbon fibers, 5 wt % CNTs, and 15 wt % PAN. The slurry was used to create a uniform carbon film via a wet film-forming method using a doctor blade. This film was then immersed in methanol, a poor solvent, inducing the formation of a porous structure through the NIPS process (Figure S8).[31,32] During this process, the introduction of a non-solvent into the polymer film leads to the formation of interconnected voids, creating a

Table 1. Surface-area and pore-volume data of porous carbon membranes

Carbon	BET surface area (m^2 g^{-1})	Mesopore diameter (nm)	Pore volume (cm^3 g^{-1}) Micro <2 nm	Small meso >2 nm	Large meso >20 nm	Macro 0.2–10 μm	Porosity (%)	Bulk density (g cm^{-3})
C-10	1411	10	0.59	3.33	1.12	2.62	92	0.15
C-16	1374	9	0.55	2.93	0.94	2.50	92	0.16
C-19	1215	9	0.46	2.83	1.09	2.63	92	0.18
C-21	883	9	0.33	2.15	0.87	2.36	91	0.20
C-24	280	–	0.11	1.19	0.77	2.53	89	0.22

BET surface-area, pore-diameter, and pore-volume data for the carbon membranes, determined from N_2 adsorption/desorption and mercury (Hg) porosimetry measurements. Mesopore and micropore volumes were calculated using the Barrett-Joyner-Halenda (BJH) and Horvath-Kawazoe (HK) methods, respectively, while macropore volume was obtained from Hg porosimetry.

sponge-like structure. This technique produced carbon membranes with a hierarchical macro-mesoporous interconnected network, expected to improve both the transport properties and capacity of the electrode. The membranes were dried and subjected to heat treatment, followed by carbonization at 1,050°C under an inert atmosphere. The resulting carbon-based membranes demonstrated high mechanical strength, maintaining their self-standing characteristics (Figure 2A).

The top-view SEM image of the as-prepared self-standing carbon membrane composed of C-21 reveals that carbon powder is uniformly distributed on the electrode surface (Figure 2B). The magnified view (Figure 2C) of Figure 2B confirms that an entangled network of carbon fibers and CNTs supports the carbon powders, providing good mechanical stability for the self-standing membrane. The cross-sectional SEM image (Figure 2D) of the membrane electrode shows the high uniformity of the membrane thickness. By applying a focused ion beam (FIB), the cross-sectional SEM images (Figures 2E and 2F) give a clearer idea about the internal bulk structure of the membrane. From these images, the formation of micro-meter-sized pores can be seen between carbon particles and a sponge-like hierarchical porous structure of the electrode.

To gain deeper insights into the pore structure of the fabricated self-standing carbon membranes, N_2 adsorption/desorption measurements were conducted along with mercury porosimetry to estimate macroporosity. The N_2 adsorption/desorption isotherms (Figure 2G) and BJH pore-size distribution curves (Figure 2H) revealed trends of BET surface area and pore volume consistent with those observed in the carbon powder samples. Specifically, a substantial reduction in both micropore (diameter <2 nm) and small mesopore (diameter 2–20 nm) volumes was observed (Figure 2I and Table 1). For instance, the micropore volume decreased dramatically from 0.59 cm^3 g^{-1} for C-10 to 0.11 cm^3 g^{-1} for C-24, reflecting a reduction of over 80%. Similarly, the small mesopore volume of C-10, measured at 3.33 cm^3 g^{-1}, dropped by more than 60% to 1.19 cm^3 g^{-1} for C-24. In contrast, the large mesopore (diameter >20 nm) volume remained relatively unaffected by increasing carbonization temperatures. Moreover, as the NIPS process was applied consistently across all samples after carbon powder preparation, the macropore volume of the self-standing carbon membranes exhibited minimal variation regardless of carbonization temperature. These findings suggest that higher carbonization temperatures selectively reduce pore volumes in the sub-20-nm range while leaving larger mesopores and macropores largely unchanged.

LOB performance test

The discharge capacities of positive electrodes made from various carbon materials were initially evaluated in coin-type cells using an excess amount of electrolyte. For this assessment, a 1 M lithium bis(trifluoromethanesulfonyl)imide (LiTFSI) solution in tetraethylene glycol dimethyl ether (TEGDME) was employed. This approach ensured that the discharge capacities were accurately measured without concerns about electrolyte depletion. The cells were discharged at a current density of 0.4 mA cm^{-2} until a cutoff voltage of 2.3 V was reached. The discharge-potential profiles (Figure 3A) for all carbon samples indicate a consistent decrease in both discharge capacity (Figure S9) and average discharge potential (Figure S10) with increasing carbonization temperature. The higher average discharge potentials observed in carbons carbonized at lower temperatures can be attributed to the catalytic activity of surface defects and oxygen functional groups during the oxygen reduction reaction (ORR).[34,35] The relationship between discharge capacity and pore volume (Figure 3B) demonstrates a clear positive correlation. This suggests that, as pore volume increases, the carbon material offers more space for accommodating Li_2O_2 as the discharge product, thereby enhancing capacity. Although high-temperature carbonization reduces both the average discharge potential and capacity, all carbon samples, except C-24, exhibited significantly high capacities (>1,300 mAh g^{-1}).

Subsequently, the carbon electrodes were subjected to repeated discharge/charge cycling experiments, excluding C-24 due to its specific capacity being below 1,000 mAh g^{-1}. Stacked-type LOB cells with a 2 × 2-cm^2 electrode area (Figure S11) were used for these tests (details provided in the methods section). The electrolyte consisted of 0.5 M LiTFSI, 0.5 M lithium nitrate ($LiNO_3$), and 0.2 M lithium bromide (LiBr) dissolved in TEGDME. To ensure an optimized lean amount of electrolyte loading, the electrolyte volume was carefully adjusted to match the pore volume of each carbon material, ensuring 100% pore filling. The electrolyte was loaded into the carbon electrodes using a vacuum impregnation method. A comparison of the electrolyte-to-carbon mass ratio (Table 2; Figure S12) shows that carbons carbonized at higher temperatures require less electrolyte for pore filling. For example, C-10 exhibits a mass ratio of 7.03, whereas C-21 has a much lower ratio of

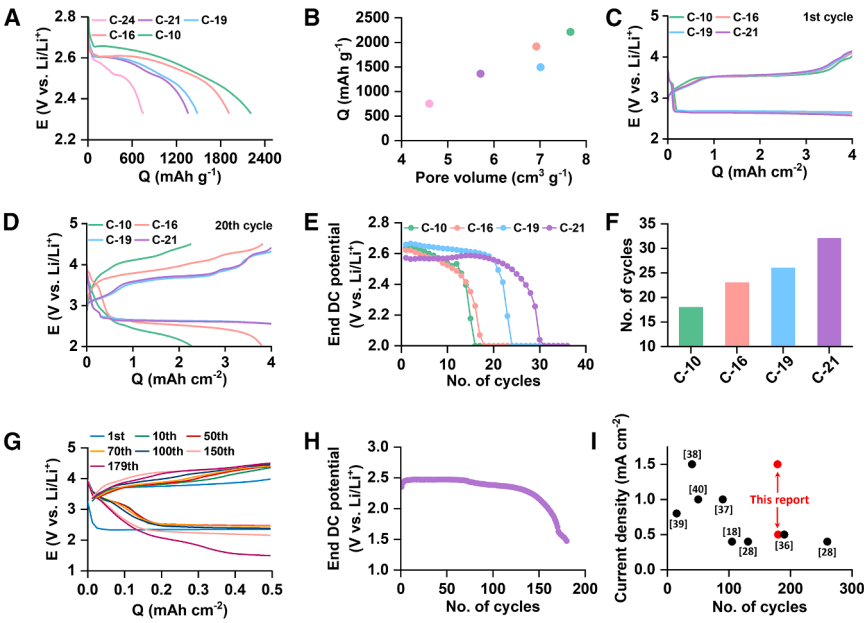

Figure 3. Galvanostatic discharge/charge cycle results of the Li-O_2 cells

(A) First galvanostatic discharge-potential profiles of all electrodes in coin cell configuration with excess electrolyte at a current density of 0.4 mA cm^{-2}.

(B–D) (B) Plot of discharge capacity versus pore volume from data in (A). Overlapped galvanostatic voltage profiles for the (C) first cycle and (D) 20th cycle of different electrodes in stacked-cell configuration with lean electrolyte under a current density of 0.4 mA cm^{-2} and limited capacity of 4 mAh cm^{-2}.

(E) Comparison of discharge potentials at the end of each cycle for different electrodes.

(F) Cycling stability of various electrodes, showing the cycle number after which the cell capacity drops below 80% of the set capacity.

(G) Galvanostatic voltage profiles for selected cycles of the stacked cell with the C-21 electrode, cycled at a current density of 1.5 mA cm^{-2} under lean-electrolyte conditions.

(H) Discharge-potential variation at the end of each cycle during cycling of the cell shown in (G).

(I) Comparison of the cycle life of the C-21 cell with previously reported cells at different current densities.

4.25, indicating a 40% reduction. The cells were cycled at a current density of 0.4 mA cm^{-2} with a capacity limitation of 4 mAh cm^{-2}. The discharge/charge profiles from the first cycle (Figure 3C) are similar across all samples, featuring a flat discharge-potential plateau between 2.5 and 2.6 V versus Li/Li^+, a sloping low-potential region during early charging, followed by a plateau around 3.5 V versus Li/Li^+, and a high-potential region above 4.0 V versus Li/Li^+ in the last 75% of the charge process. We also examined the morphologies of the discharged electrodes, and, as shown in the SEM images in Figure S13, no significant differences were observed. Despite these initially comparable profiles, cycling stability varied significantly with carbonization temperature. Discharge and charge overpotentials increased more rapidly in samples carbonized at lower temperatures (Figures S14–S17). The voltage profiles at the 20th cycle (Figure 3D) show that the discharge/charge overpotentials remained low and stable for C-19 and C-21, while they were notably higher for C-10 and C-16. A comparison of discharge potentials at the end of each cycle (Figure 3E) reveals that the C-10 and C-16 cells reached the 2-V vs. Li/Li^+ cutoff before completing 20 cycles. In contrast, cells with C-19 and C-21 reached the 2-V cutoff at 24 and 31 cycles, respectively. The results (Figure 3F) comparing the number of cycles beyond which the discharge capacity drops below 80% of the specified capacity of 4 mAh cm^{-2} indicate that the cycling stability of the electrodes improves as the carbonization temperature increases.

Following the comparative evaluation of cycling stability, which confirmed the superior performance of C-21, long-term cycling tests were conducted using C-21 in a stacked-type cell with a 2 × 2-cm^2 electrode area. For these tests, the areal capacity was set at 0.5 mAh cm^{-2}, with current densities of 0.5 and 1.5 mA cm^{-2}, corresponding to C-rates of 1 and 3, respectively. The voltage profiles for the cells cycled at 0.5 mA cm^{-2} (Figure S18) and 1.5 mA cm^{-2} (Figure 3G) demonstrated remarkable long-term cycling stability, achieving 179 cycles in both cases. Notably, the discharge potentials at the end of each cycle remained above 2.4 V versus Li/Li^+ for more than 120 cycles, even at the high current density of 1.5 mA cm^{-2} (Figure 3H). A comparison of the cycling stability of C-21 with other reported positive electrode materials (Figure 3I; Table S2) places C-21 among the top three at a cycling rate of 0.5 mA cm^{-2}.[18,28,36–40] More impressively, at 1.5 mA cm^{-2}, C-21 exhibited an unprecedented cycling stability of 179 cycles. In addition, we benchmarked C-21 against several commercially available carbon electrodes under comparable conditions, as previously reported by our group.[5] These results, presented in Table S3, further highlight the superior cycling performance of C-21. These results emphasize not only the excellent electrochemical stability of C-21 but also its outstanding rate capability. This performance is attributed to the highly stable graphitic structure of the carbon material and the hierarchical meso-macroporous architecture of the electrode membrane, which together enhance both capacity and cycling life under high-current-density conditions.

Table 2. Electrolyte loading amounts in different electrodes

Carbon electrode	Mass loading (mg cm^{-2})	Electrolyte mass (mg cm^{-2})	Electrolyte/electrode mass ratio
C-10	5.1	35.85	7.03
C-16	4.7	26.27	5.59
C-19	4.6	24.84	5.4
C-21	5.2	22.1	4.25

Electrode and electrolyte mass loading for 100% pore filling and their ratios for the cycling of different electrodes under lean-electrolyte conditions.

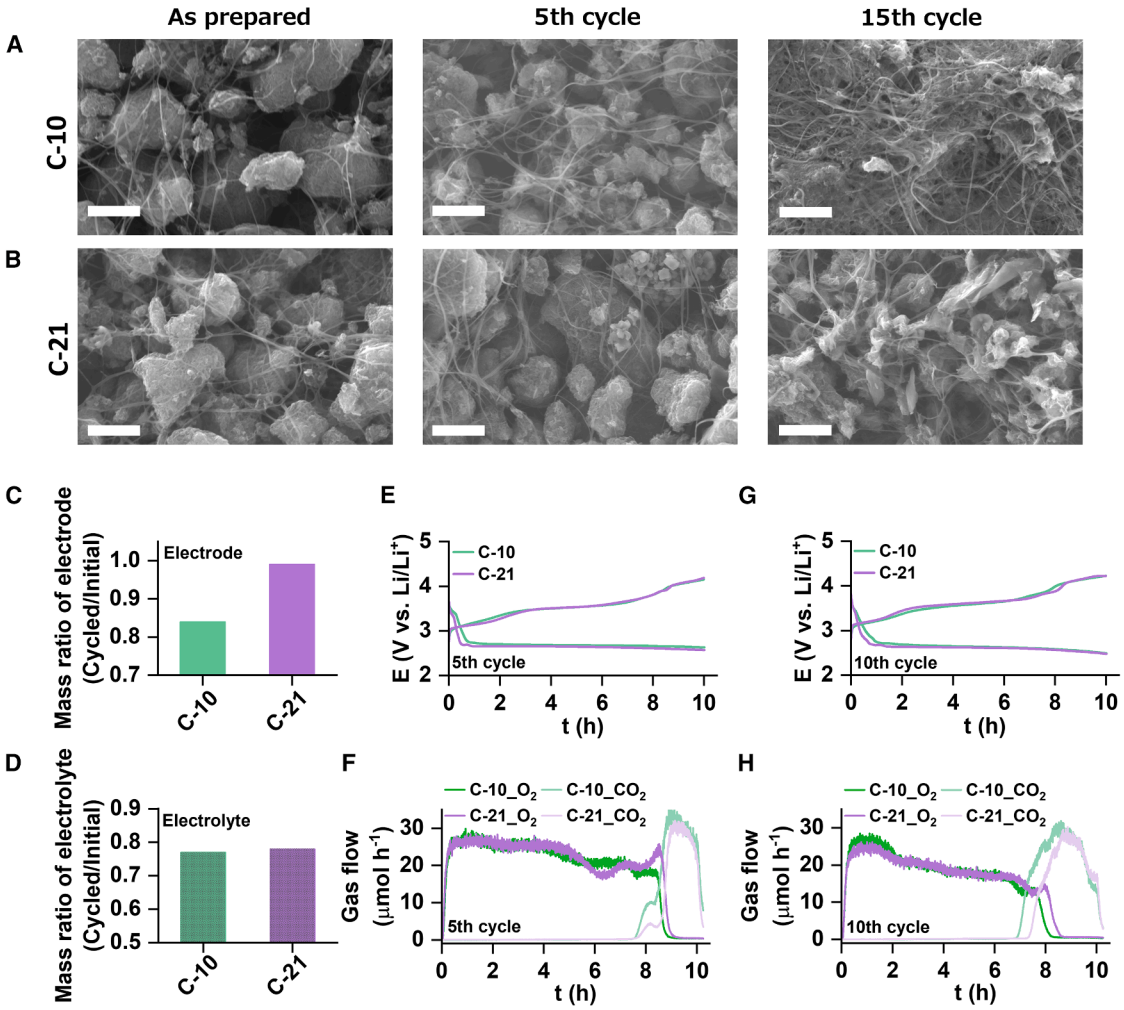

Figure 4. Postmortem analysis of cycled electrodes

(A and B) Top-view SEM images of the as-prepared and cycled (A) C-10 and (B) C-21 electrodes. Scale bars, 2 μm.

(C) Mass ratio of the cycled and initial electrodes.

(D) Ratio of the electrolyte amount recovered from the cells after cycling to the initially used amount.

(E and F) (E) Galvanostatic voltage profiles at a current density of 0.4 mA cm^{-2} and (F) gas evolution rates at the fifth cycle.

(G and H) (G) Galvanostatic voltage profiles at a current density of 0.4 mA cm^{-2} and (H) gas evolution rates at the 10th cycle.

Analysis of the degradation mechanism of LOBs

Here, our focus turns to elucidating the mechanism behind the improved cycle life of LOBs achieved by increasing the temperature during the carbonization process of the electrode materials. Specifically, in the subsequent experiments, we delve into the detailed analysis of LOB configurations utilizing C-10 and C-21 carbons as the representative electrode materials. The LOB employing C-10 exhibited a higher full-discharge capacity and required a larger initial quantity of electrolyte during the cycle test compared to that of C-21. However, the cycle life of the LOB equipped with C-10 proved inferior to that of C-21, indicating a complex degradation mechanism within the LOB system.

Guided by these observations, we investigated the changes in the morphologies of the electrodes after five and 15 cycles with a limited capacity of 4 mAh cm^{-2}. The SEM images (Figures 4A and 4B) of the pristine and cycled cells offer a comparative morphological analysis of the C-10 and C-21 electrodes. Gradual degradation of morphologies is apparent for both C-10 and C-21. However, degradation is more pronounced for C-10, as shown by the complete disappearance of particle-like morphology and noticeable collapse of the inter-particle pore structure after 15 cycles. Nevertheless, despite some degradation, C-21 managed to retain its overall morphologies after 15 cycles. These findings collectively underscore that the decomposition of carbon electrodes is markedly suppressed in LOB cells utilizing C-21 electrodes compared to those with C-10 electrodes.

Considering the degradation of the carbon electrode during cycling, we investigated changes in the mass of the carbon electrodes after 15th cycle. The electrodes underwent thorough washing with deionized water to eliminate any accumulated

Table 3. Electrode masses before and after Li-O_2 cell cycling

Carbon electrode	State of the cell	Average electrode mass (mg)	Cycled/initial mass ratio
C-10	initial	17.60	0.84
	after cycle	14.85	
C-21	initial	17.38	0.993
	after cycle	17.25	

Average masses of the pristine and cycled C-10 and C-21 electrodes and their ratios from four repeat experiments.

Table 4. Electrolyte masses before and after Li-O_2 cell cycling

Carbon electrode	State of the cell	Average electrolyte mass (mg)	Cycled/ initial mass ratio
C-10	initial	118.65	0.77
	after cycle	91.85	
C-21	initial	103.68	0.78
	after cycle	80.70	

Average masses of the electrolyte initially used and recovered from the cycled cells with C-10 and C-21 electrodes and their ratios from four repeat experiments.

solid-state byproducts, and this process provides an estimate of the mass of the unreacted carbon electrode. From the ratio of electrode masses after and before the cycling tests (Figure 4C), it is evident that the mass of the C-10 electrode decreased by approximately 16% after the cycles, a decline attributed to chemical and electrochemical oxidative corrosion of the carbon material within the LOB. Conversely, C-21 exhibited minimal change, with a mere 0.75% reduction in electrode mass. Detailed values of the electrode masses measured before and after cycling over repeated experiments and the average values can be found in Tables S4 and 3, respectively. The d-spacing values of (002) peak from XRD data (Figure S19) comparing the crystallinity of carbons before and after cycling exhibited an increase in the (002) peak d-spacing after cycling of both C-10 and C-21, indicating a loss of crystallinity. However, C-21 retained a higher degree of crystallinity compared to C-10, even after the 15th cycle.

Additionally, we quantified the remaining electrolyte solvent in the LOBs after the 15th cycle. The extracted electrolyte underwent liquid chromatography-mass spectrometry (LC-MS) analysis. The results (Figure 4D) demonstrate that, regardless of the carbon electrode, approximately 22% of the electrolyte is lost, indicating a similar extent of electrolyte degradation across all electrodes, attributable to the consistent cutoff potential and areal capacity set for all LOB cells. Comprehensive data on the electrolyte solvent masses measured before and after cycling across multiple experiments, along with their average values, are available in Tables S5 and 4, respectively.

The fundamental principle underlying LOBs involves the reversible electrochemical reduction and evolution of O_2 during discharge and charge cycles, respectively.[41] Consequently, the assessment of evolved O_2 serves as a common metric to determine the reversibility of an LOB. However, alongside the intended O_2 evolution, the occurrence of parasitic side reactions often leads to the release of CO_2 gas in LOBs.[42] Thus, to attain a comprehensive understanding of the reactions occurring within the positive electrode and to quantify the amount of gases released, we conducted an online electrochemical mass spectrometry (MS) (online MS) analysis of LOBs utilizing C-10 and C-21. The discharge/charge voltage profiles and the corresponding gas evolution rates for the fifth (Figures 4E and 4F) and 10th (Figures 4G and 4H) cycles reveal that, although both C-10 and C-21 exhibit similar voltage profiles, clear differences in gas evolution rates are evident. For instance, following the fifth cycle, the LOB employing C-21 demonstrates O_2 evolution for a longer duration with higher O_2 yield, indicative of better O_2 reversibility compared to its C-10 counterpart. As shown in Figure S20, quantitative analysis of O_2 yield at the fifth charge reveals that C-21 delivers a slightly higher yield than C-10 (67.8% vs. 65.6%). Moreover, the onset of CO_2 evolution is delayed in the C-21 cell (Figure 4F), and the total amount of CO_2 generated is substantially lower, approximately 23% less than that of C-10, as illustrated in Figure S21. These trends are consistently maintained through the 10th cycle, highlighting the enhanced stability and reduced parasitic reactions of the C-21 electrode. It is important to note that the evolved CO_2 does not necessarily correlate directly with the total mass loss of the electrode or electrolyte. Decomposition of the electrolyte and electrode materials can produce water-soluble organolithium compounds, which are removed during post-cycling rinsing and contribute to the measured mass loss. However, these species may not undergo complete electrochemical oxidation within the applied voltage window, meaning the observed CO_2 represents only a fraction of the total parasitic products formed. Despite this inconsistency, the combined quantitative data on gas evolution and electrode mass change provide compelling evidence of the superior stability and improved reversibility of the C-21 electrode.

Multi-stacked 1-Wh-class pouch-type LOB cell

The series of analytical studies clearly demonstrated the superior stability of the C-21-based carbon membrane, attributed to its high degree of graphitization. Based on these observations, we expanded our research to explore the performance of high-energy pouch-type LOB cells (Figure 5A). A six-layered, multi-stacked LOB cell with a total electrode area of 96 cm^2 (six stacks of 4 × 4 cm^2 cells, denoted as 6stack44) (Figures S22 and S23) was fabricated, and its battery performance was evaluated with a capacity limit of 4 mAh cm^{-2}. Details of the cell configuration are provided in the methods section. During the first discharge process, the LOB cell displayed stable operation with an average discharge voltage of 2.66 V versus Li/Li^+ (Figure 5B), resulting in a cell-level energy of 1.02 Wh. Owing to the limited discharge capacity and the relatively high mass of the protected Li electrode, unoptimized for maximizing specific energy, the resulting specific energy of this particular cell was approximately 130 Wh kg^{-1}. A detailed breakdown of the mass distribution of all cell components is provided in Table S6. To illustrate the full potential of the developed electrode system, we have also included

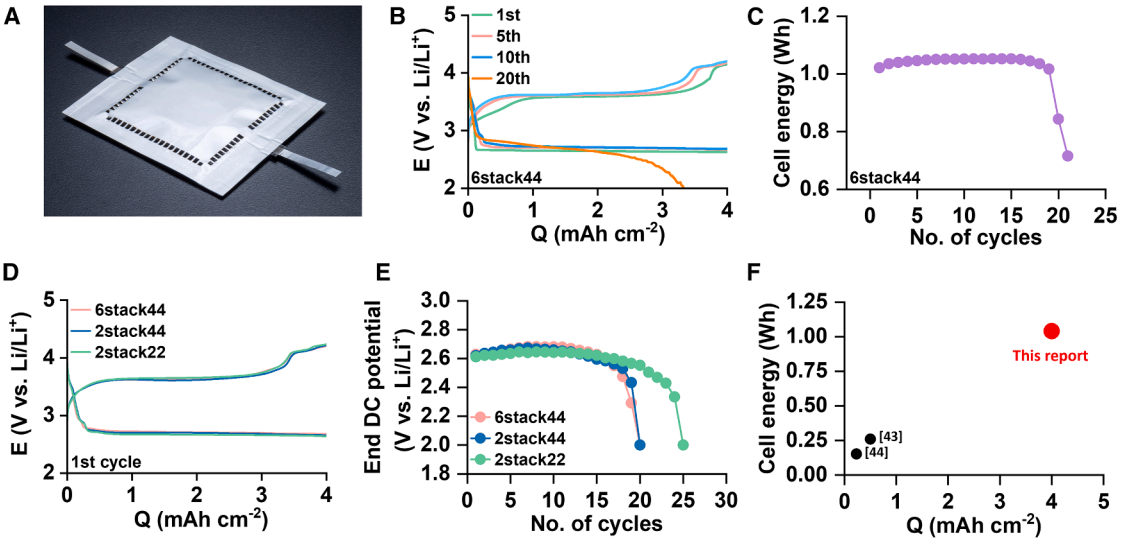

Figure 5. Galvanostatic discharge/charge cycle results of the Li-O_2 pouch cells

(A) Photographic image of the pouch cell used for multi-stack cell measurements.

(B) Galvanostatic voltage profiles for selected cycles of the 6stack44 cell at a current density of 0.4 mA cm^{-2} and limited capacity of 4 mAh cm^{-2}.

(C) Plot of cell energy versus cycle number for the 6stack44 cell.

(D) Overlapped first-cycle voltage profiles of cells with varying electrode areas and stack numbers at a current density of 0.4 mA cm^{-2} and limited capacity of 4 mAh cm^{-2}.

(E) Comparison of discharge potentials at the end of each cycle for cells with different electrode areas and stack numbers.

(F) Comparison of the cell energy and areal capacity of the present cell with previously reported cells.

simulated data in Table S7, which shows that a multi-layered cell can achieve specific energy values exceeding 700 Wh kg^{-1} under an optimized cell configuration. During charging, a stable voltage plateau was observed in the range of 3.5–3.6 V versus Li/Li^+, with the voltage eventually rising to 4.2 V. Stable discharge/charge cycling was maintained for 19 cycles, after which, during the 20th discharge, the voltage dropped sharply, reaching the cutoff condition. As a result, the cell-level energy remained at > 1 Wh for 19 cycles before dropping to 0.85 Wh at the 20th cycle (Figure 5C).

To further investigate the failure mechanisms in multi-stacked LOB cells, we fabricated additional cells with varying stack numbers and electrode sizes. Specifically, a two-layer stacked cell with a total electrode area of 32 cm^2 (two stacks of 4 × 4 cm^2, denoted as 2stack44) and a two-layer stacked cell with an area of 8 cm^2 (two stacks of 2 × 2 cm^2, denoted as 2stack22) were tested. The voltage profiles during the first discharge/charge cycles (Figure 5D) for all three configurations showed nearly identical behavior. However, performance differences became apparent with extended cycling. The 2stack22 cell maintained stable operation up to the 24th cycle, reaching the cutoff voltage during the 25th discharge (Figures 5E and S24). In contrast, the 2stack44 cell showed a notable decrease in discharge voltage by the 20th cycle (Figures 5E and S25). These results indicate that cells with larger electrodes (4 × 4 cm^2) exhibit poorer performance, likely due to inefficient horizontal oxygen transport to the center of the electrode. Notably, no significant performance difference was observed between the 2stack44 and 6stack44 cells, suggesting that increasing the number of stacks does not negatively impact battery performance. This finding underscores the innovative design of the multi-stacked cell presented in this study.

Figure 5F and Table S8 provide a summary of the performance of multi-stacked LOB cells from the literature, specifically focusing on cells with more than four layers.[43,44] Notably, only three studies, including the present work, have reported stacking-type LOBs with more than four layers. In contrast to the cell-level energy of >1 Wh achieved in this study, previously reported cells exhibited energy levels below 0.3 Wh, largely due to their limited areal capacities (<1 mAh cm^{-2}). Although LOB cells with higher areal capacities have been demonstrated, their integration into multi-stacked systems has been hindered by challenges in fabricating large-scale electrodes of sufficient quality to ensure optimal performance. The porous carbon electrodes developed in this work overcome these challenges, offering both scalability and high areal capacity. As a result, the multi-stacked LOB cell in this study delivered an impressive cell-level energy of over 1 Wh.

METHODS

Synthesis of carbons

Mesoporous carbons were prepared by following a hard-templating method using MgO as the template. Phenol resin was used as the carbon source. A mixture of phenol resin and MgO was carbonized at 900°C in N_2 atmosphere to obtain carbon-MgO composite. This composite was washed with 1 M H_2SO_4 to remove the MgO template. The resulting mesoporous carbon was heat treated at selected temperatures in N_2 atmosphere.

Preparation of self-standing carbon membrane electrode

Self-standing carbon membranes were fabricated utilizing the carbon powder samples. The fabrication involved preparation of a slurry comprising 75 wt % carbon powder, 5 wt % single-walled carbon nanotube (OCSiAl, TUBALL, CNT, average fiber diameter 1.6 nm, average length 5 μm), 5 wt % carbon fiber (Nippon Polymer Sangyo, CF, average fiber diameter 6 μm, average length 3 mm), 15 wt % polyacrylonitrile (PAN), and N-methyl-2-pyrrolidone (NMP) as a solvent for achieving uniform dispersion. The slurry was uniformly spread on a sheet using a wet film-forming method with a doctor blade to maintain consistent thickness. Subsequently, the sample underwent immersion in methanol (poor solvent) and was converted into a porous film through the NIPS method. The resulting film was then subjected to solvent removal by drying at 80°C for 10 h, followed by an infusibilization treatment at 230°C for 3 h in the atmosphere using a box-type furnace (Denken High Dental). Carbonization was carried out under N_2 flow (800 mL min^{-1}) by increasing the temperature to 1,050°C at a rate of 10°C min^{-1}, maintaining it at 1,050°C for 3 h, and allowing the sample to cool to room temperature.

Characterization of the carbon powders and the self-standing membrane electrodes

The pore structures of the samples were characterized using nitrogen adsorption/desorption measurements (3 FLEX, Micromeritics Instrument), while macropore size distributions were determined via mercury porosimetry (AutoporeIV 9505, Shimadzu). XRD patterns of the samples were obtained using an X-ray diffractometer (SmartLab, Rigaku). Further analysis of the samples was conducted using a field-emission SEM (FE-SEM; S-4800, Hitachi) and laser Raman microscopy (RamanTouch-VIS-NIR, Nanophoton). Surface properties of the carbon samples were assessed through XPS (ULVAC-PHI, VersaProbe II), and TPD measurements carried out under vacuum in a temperature range of 100°C–1,800°C using a custom-built apparatus.

Coin-type LOB cell assembly and discharge performance test

An electrolyte composed of 1 M LiTFSI (Kishida Chemical, purity >99.9%) dissolved in TEGDME (Kishida Chemical, purity >99%) served as the electrolyte for all cell tests. The water content of the electrolyte was determined to be less than 30 ppm through Karl Fischer titration. Self-standing carbon membranes were employed as the positive electrodes after undergoing vacuum drying at 100°C for 12 h. Coin-type lithium-oxygen cells were assembled in a dry room with a water content of less than 10 ppm. Assembly involved the sequential stacking of metallic lithium foil (diameter 16 mm, thickness 0.2 mm; Honjo Metal), a glass-fiber-based separator (diameter 18 mm, thickness 0.27 mm; Whatman GF-A), a carbon electrode (diameter 16 mm), and a gas-diffusion layer (diameter 16 mm, thickness 0.19 mm; TGP-H-060, Toray, Japan). Electrolyte injection into the carbon electrodes was carried out using the vacuum impregnation method. During assembly, 100 μL of electrolyte was added to the separator. The LOB cells were placed inside an oxygen-filled box, with oxygen gas continuously flowing at a rate of 80 mL min^{-1}. Electrochemical experiments were conducted using battery-test equipment (SD8, Hokuto Denoko).

Stacked-type LOB cell assembly and discharge/charge cycling test

A ternary-salt electrolyte composed of 0.5 M LiTFSI (Kishida Chemical, purity >99.9%), 0.5 M $LiNO_3$ (Sigma-Aldrich, purity 99.99% trace metals basis), and 0.2 M LiBr (Sigma-Aldrich, purity 99.995% trace metals basis) dissolved in TEGDME (Kishida Chemical, purity >99%) served as the electrolyte for all cell tests. Both $LiNO_3$ and LiBr salts were subjected to vacuum drying at 120°C for >3 days prior to electrolyte preparation to ensure dryness. The water content of the electrolyte was determined to be less than 30 ppm through Karl Fischer titration. LOB cells were assembled in a dry room with a water content of less than 10 ppm. Assembly involved sequential stacking of a lithium-metal foil (2×2 cm^2, thicknesses of 0.1 mm; Honjo Metal) attached with copper-metal foil (2×2 cm^2, thicknesses of 0.01 mm; Honjo Metal), a polyolefin-based separator (2.2×2.2 cm^2, thickness of 0.02 mm), a ceramic-based solid-state separator (LICGC, thickness of 0.90 mm; Ohara), a polyolefin-based separator (2.2×2.2 cm^2, thickness of 0.02 mm), a porous carbon electrode (2×2 cm^2), and a carbon fiber-based gas-diffusion layer (thickness of 0.19 mm, TGP-H-060, Toray) and an Ni-coated PET (polyethylene terephthalate) fiber-based current collector (thickness of 0.045 mm, SEIREN Electronics Materials). A ceramic-based solid-state separator was utilized for protecting the lithium-metal negative electrode. The ceramic-based solid-state separator was sandwiched by polyolefin-based separators, and the same electrolyte was utilized for both the positive and negative electrode sides. Electrolyte injection into carbon electrodes was conducted using the vacuum impregnation method, with 2.5 μL cm^{-2} of electrolyte added to the separator during assembly. A pressure of 100 kPa was applied to the cell by a spring coil. Electrochemical experiments were performed using a battery-test equipment (TOSCAT, Toyo System). The LOB cells were placed inside an oxygen-filled box with oxygen gas continuously flowing at a rate of 80 mL min^{-1}.

Multi-stacked-type LOB cell assembly and discharge/charge cycling test

The same ternary-salt electrolyte, used for the single stacked-type LOB cell, was employed for the multi-stacked-type LOB cells. Assembly of two-layered stacked-type LOB cell with 2×2-cm^2 electrodes involved sequential stacking of a PTFE (polytetrafluoroethylene) fiber-based gas-diffusion layer (thickness of 0.1 mm, POREFLON PTFE membrane, WP-500-100), a Ni-coated PET fiber-based current collector, a porous carbon electrode, a polyolefin-based separator, a protected lithium-metal unit, a polyolefin-based separator, a porous carbon electrode, an Ni-coated PET fiber-based current collector, and a PTFE fiber-based gas-diffusion layer. The protected lithium–metal unit is prepared by stacking an aluminum laminate film frame, a ceramic-based solid-state separator, a polyolefin-based separator, copper-metal foil attached with lithium foils for both sides, a polyolefin-based separator, a ceramic-based solid-state separator, and an aluminum laminate film frame. During stacking, 2.5 μL cm^{-2} of electrolyte was added to the

polyolefin-based separator, and then the edges of the copper-metal foil and solid electrolyte with the aluminum laminate film frame was sealed by heater. Two-layered stacked-type LOB cell with 4×4 cm^2 electrodes was fabricated by using suitably sized electrode components. For the fabrication of a six-layered stacked-type LOB cell, the stacking process was simply repeated. A pressure of 100 kPa was applied to the cell by a spring coil. Electrochemical experiments were performed using battery-test equipment (TOSCAT, Toyo System). The LOB cells were placed inside an oxygen-filled box, with oxygen gas continuously flowing at a rate of 80 mL min^{-1}.

Online MS analysis

High-resolution MS analysis was performed using an MS instrument (M-401GA, CANON ANELVA) in an online setup. A specially designed electrochemical flow cell, with an inner volume of approximately 24 mL (diameter 70 mm, depth 15 mm), was employed for the analysis. The cell utilized the same components as those described for the lithium-oxygen cells outlined earlier. Before measurement, the cells were filled with O_2 gas and subjected to a discharge process up to a discharge capacity of 4 mAh cm^{-2}. Following discharge, the test cell underwent purging with excess helium (He; 50 mL min^{-1}) for 1 min to eliminate the remaining O_2. During the charging process, gas evolution was continuously monitored using He as the carrier gas at a flow rate of 5 mL min^{-1}. For online MS analysis, the generated gases were directly fed to the MS detector through a capillary tube (internal diameter 0.05 mm, length 7 m).

Analysis of liquid phase components

Liquid chromatography was employed to analyze the organic components, while ion chromatography was utilized to quantify the ions, including inorganic materials, in the electrolyte after cycling. Following the cell cycles, the liquid electrolytes within the cathode underwent extraction with water and subsequent analysis using the Acquity H-class Ultra High-Pressure Liquid Chromatography (UPLC, Xevo G2-S QTof, Waters) system coupled with a mass spectrometer, as well as ion chromatography (ICS-2100, Dionex). To prepare the samples for chromatographic analyses, the carbon paper, cathode electrode, and cathode separator were immersed in ultrapure water, sonicated for 10 min, and then filtered. The resulting samples were appropriately diluted for each measurement. Additionally, the liquid volume of TEGDME was measured via LC-MS by extracting the electrolyte from the positive electrode in the cell post measurements.

Analysis of carbon electrodes

The electrochemically cycled carbon electrodes were evaluated against pristine electrodes through weight-loss measurement and morphological observations. Following the discharging/charging cycles, the carbon electrodes were subjected to a series of treatments. They were immersed in excess ultrapure water at 40°C for over 6 h, followed by wiping with surplus water, a process repeated multiple times. Subsequently, the electrodes were dried under vacuum and placed in an Ar-filled glovebox for a minimum of overnight before further measurements. Surface morphological analysis of the positive electrodes was conducted using a field-emission scanning electron microscope (FESEM; JSM-7800F, JEOL) equipped with an energy-dispersive X-ray spectrometer (X-MaxN 50, Oxford). Upon completion of the electrochemical measurements, the cells were disassembled within a glovebox environment. The carbon electrodes underwent initial washing with TEGDME followed by immersion in excess dry acetonitrile at 40°C for over 8 h, with surplus solvent wiped off, and this process was repeated several times. The resulting carbon electrode, containing remaining solid products, was obtained after drying in the glovebox. Sample preparation for SEM analysis was conducted within a glovebox and transferred using an unexposed vessel.

RESOURCE AVAILABILITY

Lead contact

For additional information and resources, the lead author, Shoichi Matsuda (matsuda.shoichi@nims.go.jp) should be contacted.

Materials availability

The sources of all the materials used in this study are mentioned in the methods section.

Data and code availability

- All the raw or processed data are available upon request from the lead author, Shoichi Matsuda (matsuda.shoichi@nims.go.jp).
- No code was generated or used for analysis in this work.
- Additional information necessary to reproduce or reanalyze the data presented in this study is available from the lead author upon reasonable request.

ACKNOWLEDGMENTS

This work received support from the National Institute for Materials Science (NIMS) Battery Research Platform.

AUTHOR CONTRIBUTIONS

Conceptualization, A.D., T.M., and S.M.; data curation, T.K., E.M., T.O., S.Y., J.T., Y.N., and T.M.; investigation, T.K., E.M., T.O., S.Y., J.T., Y.N., and T.M.; formal analysis, A.D., T.K., E.M., T.O., S.Y., J.T., Y.N., T.M., and S.M.; funding acquisition, T.M. and S.M.; methodology, A.D. and S.M.; project administration, T.M. and S.M.; visualization, A.D. and S.M.; supervision, T.M. and S.M.; writing – original draft, A.D. and S.M.; writing – review & editing, A.D., T.M., and S.M.

DECLARATION OF INTERESTS

The authors declare no competing interests.

SUPPLEMENTAL INFORMATION

Supplemental information can be found online at https://doi.org/10.1016/j.xcrp.2025.102841.

Received: March 11, 2025
Revised: July 2, 2025
Accepted: August 20, 2025
Published: September 17, 2025

REFERENCES

1. Matsuda, S., Yasukawa, E., Kameda, T., Kimura, S., Yamaguchi, S., Kubo, Y., and Uosaki, K. (2021). Carbon-black-based self-standing porous

electrode for 500 Wh/kg rechargeable lithium-oxygen batteries. Cell Rep. Phys. Sci. *2*, 100506. https://doi.org/10.1016/j.xcrp.2021.100506.

2. Ue, M., Sakaushi, K., and Uosaki, K. (2020). Basic knowledge in battery research bridging the gap between academia and industry. Mater. Horiz. *7*, 1937–1954. https://doi.org/10.1039/D0MH00067A.
3. MATSUDA, S. (2023). Rechargeable Lithium-Air Batteries with Practically High Energy Density. Electrochem *91*, 101006. https://doi.org/10.5796/electrochemistry.23-00061.
4. Matsuda, S., Yasukawa, E., Kimura, S., Yamaguchi, S., and Uosaki, K. (2024). Evaluation of performance metrics for high energy density rechargeable lithium–oxygen batteries. Faraday Discuss. *248*, 341–354. https://doi.org/10.1039/D3FD00082F.
5. Saengkaew, J., Kameda, T., Ono, M., and Matsuda, S. (2022). Self-standing porous carbon electrodes for lithium–oxygen batteries under lean electrolyte and high areal capacity conditions. Mater. Adv. *3*, 3536–3544. https://doi.org/10.1039/D1MA01001H.
6. Ma, S.B., Lee, D.J., Roev, V., Im, D., and Doo, S.-G. (2013). Effect of porosity on electrochemical properties of carbon materials as cathode for lithium-oxygen battery. J. Power Sources *244*, 494–498. https://doi.org/10.1016/j.jpowsour.2013.03.150.
7. Belova, A.I., Kwabi, D.G., Yashina, L.V., Shao-Horn, Y., and Itkis, D.M. (2017). Mechanism of Oxygen Reduction in Aprotic Li–Air Batteries: The Role of Carbon Electrode Surface Structure. J. Phys. Chem. C *121*, 1569–1577. https://doi.org/10.1021/acs.jpcc.6b12221.
8. Xiao, J., Wang, D., Xu, W., Wang, D., Williford, R.E., Liu, J., and Zhang, J.-G. (2010). Optimization of Air Electrode for Li/Air Batteries. J. Electrochem. Soc. *157*, A487. https://doi.org/10.1149/1.3314375.
9. Dutta, A., Wong, R.A., Park, W., Yamanaka, K., Ohta, T., Jung, Y., and Byon, H.R. (2018). Nanostructuring one-dimensional and amorphous lithium peroxide for high round-trip efficiency in lithium-oxygen batteries. Nat. Commun. *9*, 680. https://doi.org/10.1038/s41467-017-02727-2.
10. Dutta, A., Ito, K., and Kubo, Y. (2021). Nanoconfined growth of lithium-peroxide inside electrode pores: a noncatalytic strategy toward mitigating capacity–rechargeability trade-off in lithium–air batteries. Mater. Adv. *2*, 1302–1312. https://doi.org/10.1039/D0MA00979B.
11. Xie, J., Yao, X., Cheng, Q., Madden, I.P., Dornath, P., Chang, C.-C., Fan, W., and Wang, D. (2015). Three Dimensionally Ordered Mesoporous Carbon as a Stable, High-Performance Li–O_2 Battery Cathode. Angew. Chem. Int. Ed. *54*, 4299–4303. https://doi.org/10.1002/anie.201410786.
12. Lin, X., Zhou, L., Huang, T., and Yu, A. (2013). Hierarchically porous honeycomb-like carbon as a lithium–oxygen electrode. J. Mater. Chem. A *1*, 1239–1245. https://doi.org/10.1039/C2TA00236A.
13. Zhou, W., Zhang, H., Nie, H., Ma, Y., Zhang, Y., and Zhang, H. (2015). Hierarchical Micron-Sized Mesoporous/Macroporous Graphene with Well-Tuned Surface Oxygen Chemistry for High Capacity and Cycling Stability Li–O_2 Battery. ACS Appl. Mater. Interfaces *7*, 3389–3397. https://doi.org/10.1021/am508513m.
14. Wang, Z.-L., Xu, D., Xu, J.-J., Zhang, L.-L., and Zhang, X.-B. (2012). Graphene Oxide Gel-Derived, Free-Standing, Hierarchically Porous Carbon for High-Capacity and High-Rate Rechargeable Li-O_2 Batteries. Adv. Funct. Mater. *22*, 3699–3705. https://doi.org/10.1002/adfm.201200403.
15. Sun, B., Huang, X., Chen, S., Munroe, P., and Wang, G. (2014). Porous Graphene Nanoarchitectures: An Efficient Catalyst for Low Charge-Overpotential, Long Life, and High Capacity Lithium–Oxygen Batteries. Nano Lett. *14*, 3145–3152. https://doi.org/10.1021/nl500397y.
16. Zhang, Z., Bao, J., He, C., Chen, Y., Wei, J., and Zhou, Z. (2014). Hierarchical Carbon–Nitrogen Architectures with Both Mesopores and Macrochannels as Excellent Cathodes for Rechargeable Li–O_2 Batteries. Adv. Funct. Mater. *24*, 6826–6833. https://doi.org/10.1002/adfm.201401581.
17. Liu, H., Liu, X., Li, W., Guo, X., Wang, Y., Wang, G., and Zhao, D. (2017). Porous Carbon Composites for Next Generation Rechargeable Lithium Batteries. Adv. Energy Mater. *7*, 1700283. https://doi.org/10.1002/aenm.201700283.
18. Luo, W.-B., Chou, S.-L., Wang, J.-Z., Zhai, Y.-C., and Liu, H.-K. (2015). A Metal-Free, Free-Standing, Macroporous Graphene@g-C_3N_4 Composite Air Electrode for High-Energy Lithium Oxygen Batteries. Small *11*, 2817–2824. https://doi.org/10.1002/smll.201403535.
19. Albertus, P., Girishkumar, G., McCloskey, B., Sánchez-Carrera, R.S., Kozinsky, B., Christensen, J., and Luntz, A.C. (2011). Identifying Capacity Limitations in the Li/Oxygen Battery Using Experiments and Modeling. J. Electrochem. Soc. *158*, A343. https://doi.org/10.1149/1.3527055.
20. Jung, J.-W., Cho, S.-H., Nam, J.S., and Kim, I.-D. (2020). Current and future cathode materials for non-aqueous Li-air (O_2) battery technology – A focused review. Energy Storage Mater. *24*, 512–528. https://doi.org/10.1016/j.ensm.2019.07.006.
21. Kim, M., Yoo, E., Ahn, W.-S., and Shim, S.E. (2018). Controlling porosity of porous carbon cathode for lithium oxygen batteries: Influence of micro and meso porosity. J. Power Sources *389*, 20–27.
22. Hanzawa, Y., Hatori, H., Yoshizawa, N., and Yamada, Y. (2002). Structural changes in carbon aerogels with high temperature treatment. Carbon *40*, 575–581. https://doi.org/10.1016/S0008-6223(01)00150-6.
23. Wang, Y., and Hao, L. (2024). The limitation mechanisms on the discharge behavior of Li-O_2 batteries. J. Electroanal. Chem. *955*, 118064. https://doi.org/10.1016/j.jelechem.2024.118064.
24. Mirzaeian, M., and Hall, P.J. (2009). Preparation of controlled porosity carbon aerogels for energy storage in rechargeable lithium oxygen batteries. Electrochim. Acta *54*, 7444–7451. https://doi.org/10.1016/j.electacta.2009.07.079.
25. Wong, R.A., Dutta, A., Yang, C., Yamanaka, K., Ohta, T., Nakao, A., Waki, K., and Byon, H.R. (2016). Structurally Tuning Li_2O_2 by Controlling the Surface Properties of Carbon Electrodes: Implications for Li–O_2 Batteries. Chem. Mater. *28*, 8006–8015. https://doi.org/10.1021/acs.chemmater.6b03751.
26. Dutta, A., Ito, K., Nomura, A., and Kubo, Y. (2020). Quantitative Delineation of the Low Energy Decomposition Pathway for Lithium Peroxide in Lithium–Oxygen Battery. Adv. Sci. *7*, 2001660. https://doi.org/10.1002/advs.202001660.
27. Ono, M., Saengkaew, J., and Matsuda, S. (2023). Poor Cycling Performance of Rechargeable Lithium–Oxygen Batteries under Lean-Electrolyte and High-Areal-Capacity Conditions: Role of Carbon Electrode Decomposition. Adv. Sci. *10*, 2300896. https://doi.org/10.1002/advs.202300896.
28. Yu, W., Shen, Z., Yoshii, T., Iwamura, S., Ono, M., Matsuda, S., Aoki, M., Kondo, T., Mukai, S.R., Nakanishi, S., and Nishihara, H. (2024). Hierarchically Porous and Minimally Stacked Graphene Cathodes for High-Performance Lithium–Oxygen Batteries. Adv. Energy Mater. *14*, 2303055. https://doi.org/10.1002/aenm.202303055.
29. Morishita, T., Tsumura, T., Toyoda, M., Przepiórski, J., Morawski, A.W., Konno, H., and Inagaki, M. (2010). A review of the control of pore structure in MgO-templated nanoporous carbons. Carbon *48*, 2690–2707. https://doi.org/10.1016/j.carbon.2010.03.064.
30. Saengkaew, J., Kameda, T., Ono, M., Mizuki, E., Nagaishi, S., Iwamura, S., Mukai, S.R., and Matsuda, S. (2023). Carbon Gel-Based Self-Standing Membranes as the Positive Electrodes of Lithium–Oxygen Batteries under Lean-Electrolyte and High-Areal-Capacity Conditions. J. Phys. Chem. C *127*, 939–948. https://doi.org/10.1021/acs.jpcc.2c06979.
31. Wang, J., He, Y., Wu, Q., Zhang, Y., Li, Z., Liu, Z., Huo, S., Dong, J., Zeng, D., and Cheng, H. (2019). A facile non-solvent induced phase separation process for preparation of highly porous polybenzimidazole separator for lithium metal battery application. Sci. Rep. *9*, 19320. https://doi.org/10.1038/s41598-019-55865-6.
32. Peinemann, K.-V., Abetz, V., and Simon, P.F.W. (2007). Asymmetric superstructure formed in a block copolymer via phase separation. Nat. Mater. *6*, 992–996. https://doi.org/10.1038/nmat2038.
33. Li, Z., Deng, L., Kinloch, I.A., and Young, R.J. (2023). Raman spectroscopy of carbon materials and their composites: Graphene, nanotubes and

fibres. Prog. Mater. Sci. *135*, 101089. https://doi.org/10.1016/j.pmatsci.2023.101089.

34. Huang, S., Fan, W., Guo, X., Meng, F., and Liu, X. (2014). Positive Role of Surface Defects on Carbon Nanotube Cathodes in Overpotential and Capacity Retention of Rechargeable Lithium–Oxygen Batteries. ACS Appl. Mater. Interfaces *6*, 21567–21575. https://doi.org/10.1021/am506564n.
35. Xia, G., Shen, S., Zhu, F., Xie, J., Hu, Y., Zhu, K., and Zhang, J. (2015). Effect of oxygen-containing functional groups of carbon materials on the performance of Li–O_2 batteries. Electrochem. Commun. *60*, 26–29. https://doi.org/10.1016/j.elecom.2015.07.011.
36. Song, M., Tan, H., Li, X., Tok, A.I.Y., Liang, P., Chao, D., and Fan, H.J. (2020). Atomic-Layer-Deposited Amorphous MoS_2 for Durable and Flexible Li–O_2 Batteries. Small Methods *4*, 1900274. https://doi.org/10.1002/smtd.201900274.
37. Guo, F., Kang, T., Liu, Z., Tong, B., Guo, L., Wang, Y., Liu, C., Chen, X., Zhao, Y., Shen, Y., et al. (2019). Advanced Lithium Metal–Carbon Nanotube Composite Anode for High-Performance Lithium–Oxygen Batteries. Nano Lett. *19*, 6377–6384. https://doi.org/10.1021/acs.nanolett.9b02560.
38. Lee, Y.J., Park, S.H., Kim, S.H., Ko, Y., Kang, K., and Lee, Y.J. (2018). High-Rate and High-Areal-Capacity Air Cathodes with Enhanced Cycle Life Based on RuO_2/MnO_2 Bifunctional Electrocatalysts Supported on CNT for Pragmatic Li–O_2 Batteries. ACS Catal. *8*, 2923–2934. https://doi.org/10.1021/acscatal.8b00248.
39. Liang, Z., and Lu, Y.-C. (2016). Critical Role of Redox Mediator in Suppressing Charging Instabilities of Lithium–Oxygen Batteries. J. Am. Chem. Soc. *138*, 7574–7583. https://doi.org/10.1021/jacs.6b01821.
40. Gao, X., Chen, Y., Johnson, L.R., Jovanov, Z.P., and Bruce, P.G. (2017). A rechargeable lithium–oxygen battery with dual mediators stabilizing the carbon cathode. Nat. Energy *2*, 17118. https://doi.org/10.1038/nenergy.2017.118.
41. McCloskey, B.D., Scheffler, R., Speidel, A., Girishkumar, G., and Luntz, A.C. (2012). On the Mechanism of Nonaqueous Li–O_2 Electrochemistry on C and Its Kinetic Overpotentials: Some Implications for Li–Air Batteries. J. Phys. Chem. C *116*, 23897–23905. https://doi.org/10.1021/jp306680f.
42. McCloskey, B.D., Speidel, A., Scheffler, R., Miller, D.C., Viswanathan, V., Hummelshøj, J.S., Nørskov, J.K., and Luntz, A.C. (2012). Twin Problems of Interfacial Carbonate Formation in Nonaqueous Li–O_2 Batteries. J. Phys. Chem. Lett. *3*, 997–1001. https://doi.org/10.1021/jz300243r.
43. Kubo, Y., and Ito, K. (2014). Multicell Stack of Nonaqueous Lithium–Air Batteries. ECS Trans. *62*, 129–135. https://doi.org/10.1149/06201.0129ecst.
44. Yeon, S.-H., Shin, K.-H., Jin, C.-S., Park, S.-K., Hwang, S.H., Kim, D.H., Jeon, M.-S., Kim, S.-O., Hong, D., and Choi, Y. (2023). Optimal and systematic design of large-scale electrodes for practical Li–air batteries. Electrochim. Acta *439*, 141642. https://doi.org/10.1016/j.electacta.2022.141642.